We are IntechOpen,
the world's leading publisher of
Open Access books
Built by scientists, for scientists

6,900
Open access books available

185,000
International authors and editors

200M
Downloads

Our authors are among the

154
Countries delivered to

TOP 1%
most cited scientists

12.2%
Contributors from top 500 universities

CLARIVATE ANALYTICS
BOOK CITATION INDEX
INDEXED

WEB OF SCIENCE™

Selection of our books indexed in the Book Citation Index
in Web of Science™ Core Collection (BKCI)

Interested in publishing with us?
Contact book.department@intechopen.com

Numbers displayed above are based on latest data collected.
For more information visit www.intechopen.com

Gas-Solid Heat and Mass Transfer Intensification in Rotating Fluidized Beds in a Static Geometry

Juray De Wilde

Université catholique de Louvain, Dept. Materials and Process Engineering (IMAP), Place Sainte Barbe 2, Réaumur building, 1348 Louvain-la-Neuve, Tel.: +32 10 47 2323, Fax: +32 10 47 4028, e-mail: Juray.DeWilde@UCLouvain.be
Belgium

1. Introduction

In different types of reactors, gas and solid particles are brought into contact and gas-solid mass and heat transfer is to be optimized. This is for example the case with heterogeneous catalytic reactions, the porous solid particle providing the catalytic sites and the reactants having to transfer from the bulk flow to the solid surface from where they can diffuse into the pores of the catalyst [Froment et al., 2010]. Gas-solid heat transfer can, for example, be required to provide the heat for endothermic reactions taking place inside the solid catalyst. Intra-particle mass transfer limitations can be encountered as well, but this chapter will focus on interfacial mass and heat transfer. The overall rate of reaction is on the one hand determined by the intrinsic reaction rate, which depends on the catalyst used, and on the other hand by the rates of mass and heat transfer, which depends on the reactor configuration and operating conditions used. Hence, the optimal use of a catalyst requires a reactor in which conditions can be generated allowing sufficiently fast mass and heat transfer. This is not always possible and usually an optimization is carried out accounting for pressure drop and stability limitations. This chapter focuses on fluidized bed type reactors and the limitations of conventional fluidized beds will be explained in more detail in the next section.

To gain some insight in where gas-solid mass and heat transfer limitations come from, consider the flux expression for one-dimensional diffusion of a component A over a film around the solid particle in which the resistance for fluid-to-particle interfacial mass and heat transfer is localized:

$$N_A = -C_t D_{Am} \frac{dy_A}{dz} + y_A \left(N_A + N_B + N_R + N_S + ... \right) \tag{1}$$

In (1), a mean binary diffusivity for species A through the mixture of other species is introduced. For the calculation of the mean binary diffusivity, see Froment et al. [2010]. When a chemical reaction

$$aA + bB + ... \Leftrightarrow rR + sS + ... \tag{2}$$

takes place, the fluxes of the different components are related through the reaction stoichiometry, so that (1) becomes:

$$N_A = -C_t D_{Am} \frac{dy_A}{dz} + y_A N_A \left(1 + \frac{b}{a} - \frac{r}{a} - \frac{s}{a} - ...\right) \tag{3}$$

Solving (3) for N_A:

$$N_A = \frac{-C_t D_{Am}}{1 + \delta_A y_A} \frac{dy_A}{dz} \tag{4}$$

with

$$\delta_A = \frac{r + s + ... - a - b - ...}{a} \tag{5}$$

Integrating (4) over the (unknown) film thickness L for steady state diffusion and using an average constant value for the mean binary diffusivity results in:

$$N_A = \left(\frac{C_t D_{Am}}{L}\right) \frac{y_{A0} - y_A(L)}{y_{fA}} \tag{6}$$

where the film factor, y_{fA}, accounting for non-equimolar counter-diffusion, has been introduced:

$$y_{fA} = \frac{\left(1 + \delta_A y_A\right) - \left(1 + \delta_A y_{As}^s\right)}{\ln \frac{1 + \delta_A y_A}{1 + \delta_A y_{As}^s}} \tag{7}$$

Expression (6) shows the importance of the film thickness, L, which depends on the reactor design and the operating conditions. This implies a difficulty for the practical use of (6). In practice, gas-solid mass and heat transfer are modeled in terms of a mass, respectively heat transfer coefficient, noted k_g and h_f. For interfacial mass transfer:

$$N_A = k_g \left(y_A - y_{As}^s\right) = \frac{k_g^0}{y_{fA}} \left(y_A - y_{As}^s\right) \tag{8}$$

where the film factor was factored out, introducing the interfacial mass transfer coefficient for equimolar counter-diffusion, k_g^0. For interfacial heat transfer, the heat flux is written as:

$$Q_A = h_f \left(T - T_s^s\right) \tag{9}$$

For the calculation of k_g^0, correlations in terms of the j_D factor are typically used:

$$k_g^0 = \frac{j_D G}{M_m} Sc^{-2/3} \tag{10}$$

where Sc is the Schmidt number defined as

$$Sc = \frac{\mu}{\rho_f D_{Am}} \tag{11}$$

and G is the superficial fluid mass flux through the particle bed:

$$G = \varepsilon_g \rho_g (u - v) \tag{12}$$

Comparing (8) and (10) to (6), it is seen that the mean binary diffusivity is enclosed in Sc. The film thickness, L, is accounted for via the j_D factor which is correlated in terms of the Reynolds number:

$$j_D = f(\mathrm{Re}_p) \tag{13}$$

with Re_P the particle based Reynolds number:

$$\mathrm{Re}_p = \frac{d_p G}{\mu} \tag{14}$$

In a similar way, the heat transfer coefficient h_f is usually modeled in terms of the j_H factor and the Prandtl number which contains the fluid conductivity:

$$h_f = j_H c_P G \mathrm{Pr}^{-2/3} \tag{15}$$

with

$$j_H = f(\mathrm{Re}_p) \tag{16}$$

and

$$\mathrm{Pr} = \mu c_P / \lambda \tag{17}$$

Correlations (13) and (16) depend on the reactor type and design - see Froment et al. [2010] and Schlünder [1978] for a comprehensive discussion. For conventional, gravitational fluidized beds, Perry and Chilton [1984] proposed, for example,

$$\mathrm{Re}_p = 2.05 \mathrm{Re}_p^{-0.468} \tag{18}$$

Balakrishnan and Pei [1975] proposed:

$$j_H = 0.043 \left[\frac{d_p g}{(\varepsilon_g u)^2} \frac{(\rho_s - \rho_g) \varepsilon_s^2}{\rho_g} \right]^{0.25} \tag{19}$$

Expressions (10)-(19) show in particular the importance of earth gravity, the particle bed density, and the gas-solid slip velocity for the value of the gas-solid heat and mass transfer coefficients.

2. The limitations of conventional fluidized beds

In conventional gravitational fluidized beds, particles are fluidized against gravity, a constant on earth. This limits the window of operating conditions at which gravitational fluidized beds can be operated. The fluidization behavior depends on the type of particles that are fluidized. The typical fluidization behavior of fine particles is illustrated in Figure 1.
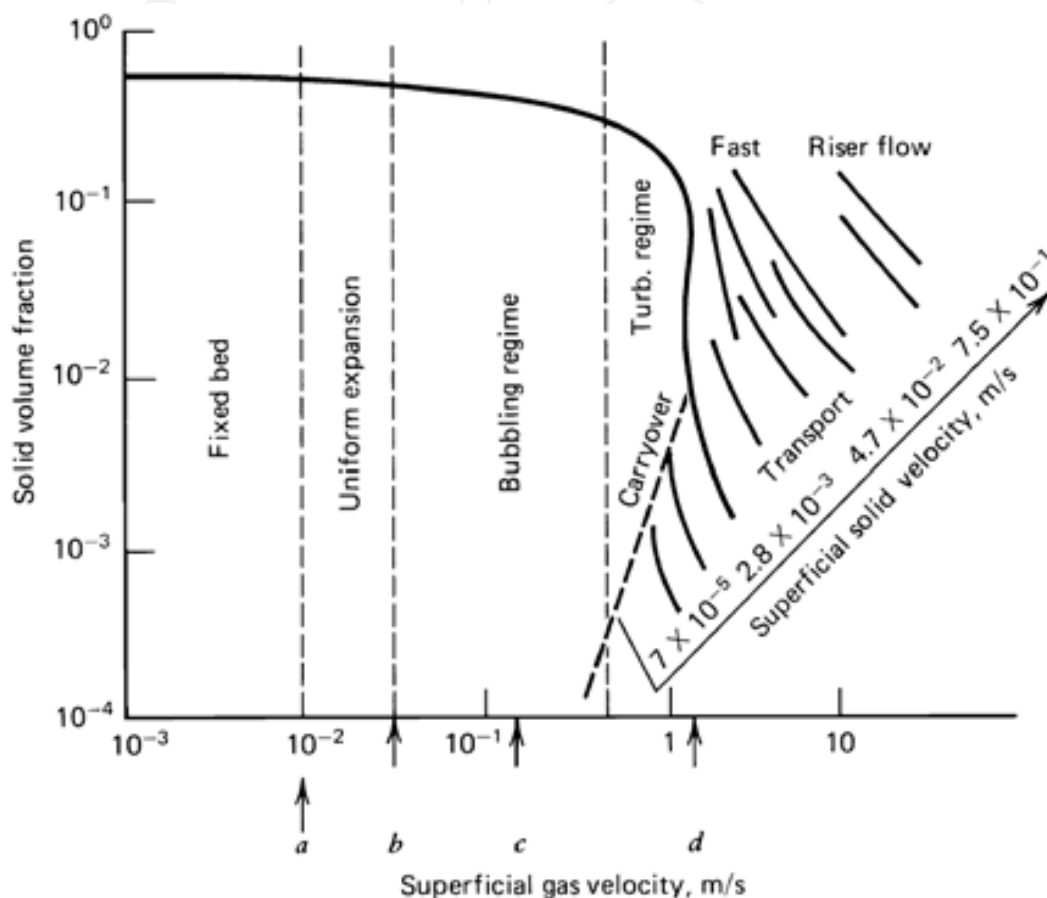

Fig. 1. Fluidization regimes with fine particles. (a) Minimum fluidization velocity; (b) Minimum bubbling; (c) Terminal velocity; (d) Blowout velocity. From Froment et al. [2010] after Squires et al. [1985].

The particle bed is fluidized when the gas-solid slip velocity exceeds the minimum fluidization velocity of the particles. When increasing the gas velocity, the uniformly fluidized state becomes unstable and bubbles appear (Figure 2). These meso-scale non-uniformities are detrimental for the gas-solid contact, but their dynamic behavior improves mixing in the particle bed. Further improvement of the gas-solid contact and the particle bed mixing can be achieved by further increasing the gas velocity and entering into the so-called turbulent regime. The gas-solid slip velocity can not be increased beyond the terminal velocity of the particles, which naturally depends on the gravity field in which the particles are suspended. Particles are then entrained by the gas and a transport regime is reached, meaning the particles are transported with the gas through the reactor. Meso-scale non-uniformities here appear under the form of clusters (Figure 2). The limitation of the gas-solid slip velocity implies limitations on the gas-solid mass and heat transfer.
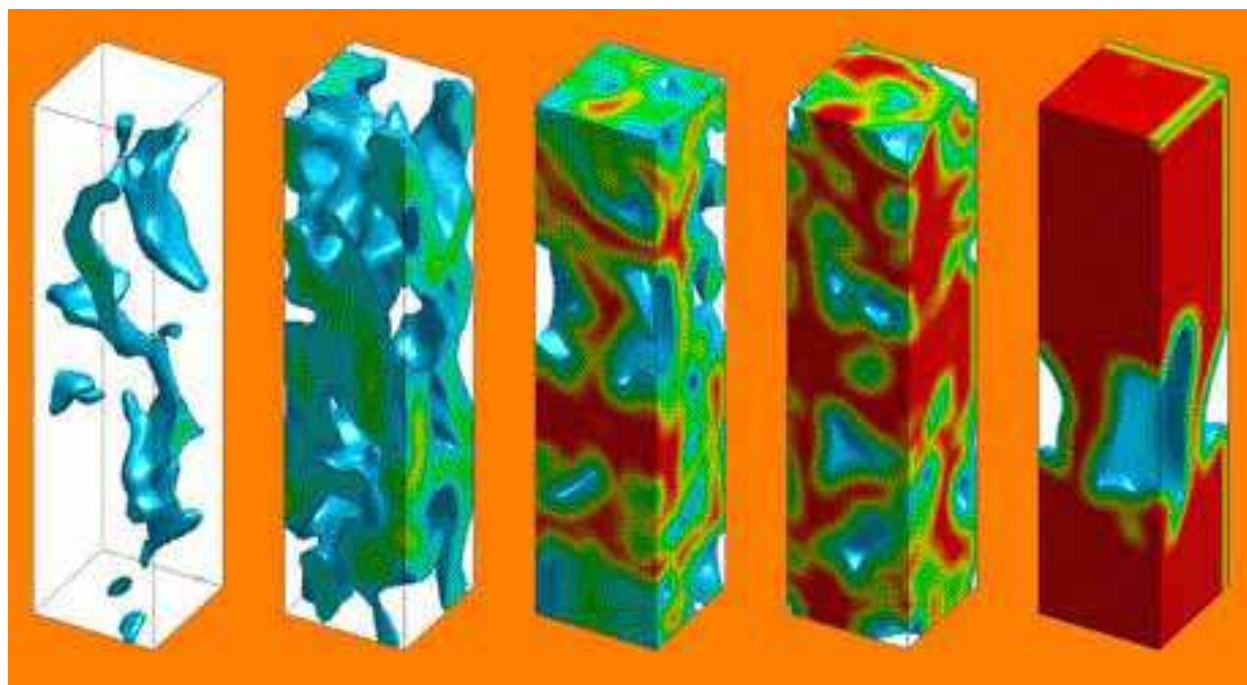
Fig. 2. Non-uniformity in the particle distribution. Appearance of bubbles and clusters. From Agrawal et al. [2001].

Macro- to reactor-scale non-uniformities have to be avoided, as they imply complete bypassing of the solids by the gas. In gravitational fluidized beds operated in a non-transport regime, this requires a certain weight of particles above the gas distributor and limits the particle bed width-to-height ratio. This on its turn introduces a constraint on the fluidization gas flow rate that can be handled per unit volume particle bed. In the transport regime, particles have to be returned from the top of the reactor to the bottom. The driving force is the weight of particles in a stand pipe and, hence, the latter should be sufficiently tall. The reactor length has to be adapted accordingly, resulting in very tall reactors. The riser reactors used in FCC, for example, are 30 to 40 m tall. The resulting gas phase and catalyst residence times in some applications limit the catalyst activity.

An important characteristic of the fluidized bed state is the particle bed density. It is directly related to the process intensity that can be reached in the reactor. The process intensity for a given reactor can be defined as how much reactant is converted per unit time and per unit reactor volume. Typically, as the gas velocity is increased, the particle bed expands and the particle bed density decreases. In a transport regime, the average particle bed density decreases significantly. In the riser regime, for example, the reactor is typically operated at 5 vol% solids or less. The process intensity is correspondingly low.

A final important limitation of gravitational fluidized beds comes from the type of particles that can be fluidized. Nano- and micro-scale particles can not be properly fluidized, the Van der Waals forces becoming too important compared to the other forces determining the fluidized bed state, i.e. the weight of the particles and the gas-solid drag force.

Most of the above mentioned limitations of gravitational fluidized beds can be removed by replacing earth gravity with a stronger force - so-called high-G operation. This has led to the development of the cylindrically shaped so-called rotating fluidized beds. A first technology of this type is based on a fluidization chamber which rotates fast around its axis of symmetry by means of a motor [Fan et al., 1985; Chen, 1987]. The moving geometry

complicates sealing and continuous feeding and removal of solids and introduces additional challenges related to vibrations. Nevertheless, rotating fluidized beds have been shown successful in removing the limitations of gravitational fluidized beds and, for example, allow the fluidization of micro- and nano-particles [Qian et al., 2001; Watano et al., 2003; Quevedo et al., 2005].

In this chapter, a novel technology is focused on that allows taking advantage of high-G operation in a static geometry. The gas-solid heat and mass transfer properties and the particle bed temperature uniformity are numerically and experimentally studied. The process intensification is illustrated for the drying of biomass and for FCC.

3. The rotating fluidized beds in a static geometry

3.1 Technology description

Figure 3 shows a schematic representation of a rotating fluidized bed in a static geometry (RFB-SG) [de Broqueville, 2004; De Wilde and de Broqueville, 2007, 2008], a vortex chamber [Kochetov et al., 1969; Anderson et al., 1971; Folsom, 1974] based technology. The unique characteristic of the technology is the way the rotational motion of the particle bed is driven, i.e. by the tangential introduction of the fluidization gas in the fluidization chamber through multiple inlet slots in its outer cylindrical wall. As a result, the particle bed is, or better can be, fluidized in two directions. The fluidization gas is forced to leave the fluidization chamber via a centrally positioned chimney. The radial fluidization of the particle bed is then controlled by the radial gas-solid drag force and the solid particles inertia. In a coordinate system rotating with the particle bed, the latter appears as the centrifugal and Coriolis forces. Radial fluidization of the particle bed is, however, not essential to take fully advantage of high-G operation. What is essential for intensifying gas-solid mass and heat transfer is the increased gas-solid slip velocity at which the bed can be operated while maintaining a high particle bed density and being fluidized.
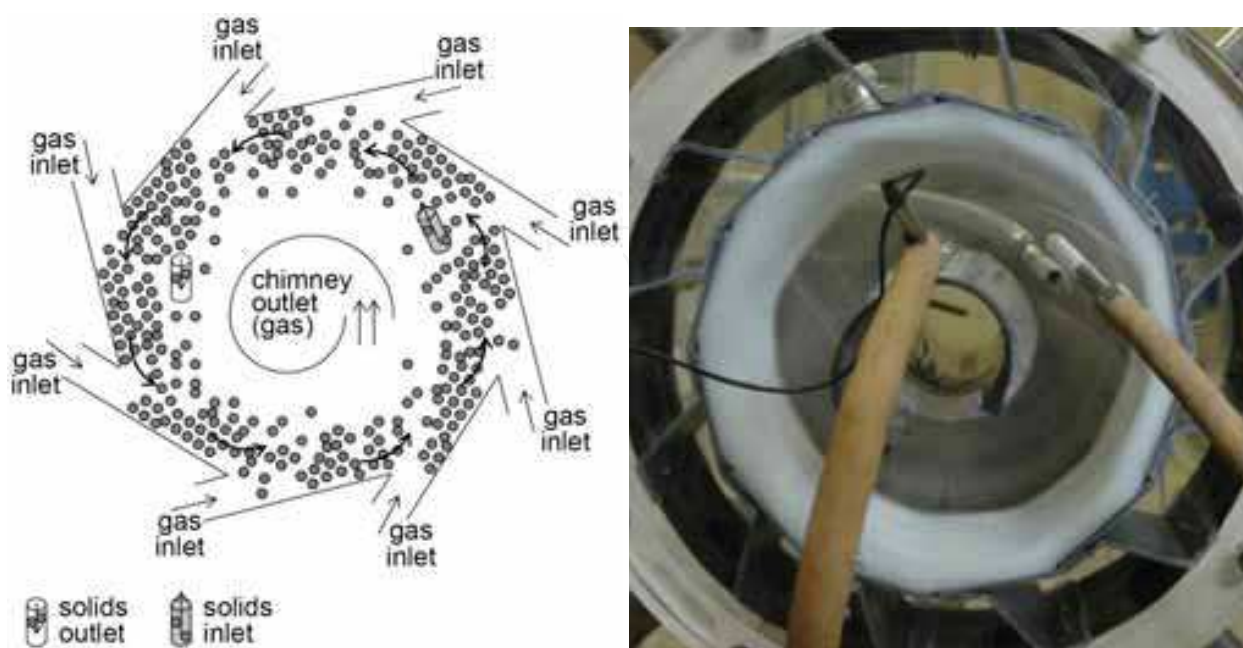

Fig. 3. The rotating fluidized bed in a static geometry. Picture from De Wilde and de Broqueville [2007].

Whether the particle bed will be radially fluidized depends mainly on the type of particles and on the fluidization chamber design, including the fluidization chamber and chimney diameters and the number and size of the gas inlets slots. At fluidization gas flow rates sufficiently high to operate high-G, the influence of the fluidization gas flow rate on the radial fluidization of the particle bed is marginal. This flexibility in the fluidization gas flow rate is an important and unique feature of rotating fluidized beds in a static geometry [De Wilde and de Broqueville, 2007, 2008, 2008b]. The explanation for this comes from the similar influence of the fluidization gas flow rate on the radial gas-solid drag force and the counteracting solid phase inertial forces resulting from the particle bed rotational motion. Experimental observations confirm the absence of radial bed expansion when increasing the fluidization gas flow rate. In some cases, even a radial bed contraction was observed.

Another important characteristic of rotating fluidized beds in a static geometry is the excellent particle bed mixing, resulting from the particle bed rotational motion and the fluctuations in the velocity field of the particles. The particle bed mixing properties were studied by De Wilde [2009] by means of a step response technique with colored particles and a close to well-mixed behavior was demonstrated at sufficiently high fluidization gas flow rates. It should be remarked that the gas phase is hardly mixed and follows a plug flow type pattern.

3.2 Theoretical evaluation of the intensification of gas-solid heat and mass transfer

As mentioned in Section 2 of this chapter, in fluidized beds, the gas-solid slip velocity, essential for the value of the gas-solid heat and mass transfer coefficient - see (10), (12), and (15), can not increase beyond the terminal velocity of the particles. An expression for the latter has been derived for gravitational fluidized beds [Froment et al., 2010] and can be extended to fluidization in a high-G field as:

$$u^{term} = \sqrt{\frac{4c \cdot d_p(\rho_s - \rho_g)}{3\rho_g C_D}} \tag{20}$$

with c the high-G acceleration. The value of the drag coefficient, C_D, depends on the particle Reynolds number, Re_p. For Re_p below 1000:

$$C_D = \frac{24}{Re_p}\left(1 + 0.15Re_p^{0.687}\right) \tag{21}$$

with, for spherical particles:

$$Re_p = \frac{|\bar{u} - \bar{v}|\varepsilon_g \rho_g d_p}{\mu} \tag{22}$$

, similar to (14). For higher Re_p:

$$C_D = 0.44 \tag{23}$$

A unique characteristic of rotating fluidized beds in a static geometry is that the high-G acceleration appearing in (20) depends on the fluidization gas flow rate and, hence, on the gas velocity u. An estimation of the high-G acceleration can be calculated from an expression derived by de Broqueville and De Wilde [2009]. Assuming a solid body type motion of the particle bed and neglecting the contribution of the Coriolis effect:

$$c = \omega^2 r = \left(\frac{2 \cdot F_g \cdot \langle n \rangle \cdot \left(\langle v^{\tan g} \rangle \big/ \langle u^{\tan g} \rangle \right)}{\langle \varepsilon_g \rangle \cdot \left(R^2 - R_f^2 \right) \cdot L} \right)^2 r \tag{24}$$

where r is the radial position in the particle bed, F_g is the fluidization gas flow rate, <n> is the average number of rotations made by the fluidization gas in the particle bed, <ε_g> is the average particle bed void fraction, R is the outer fluidization chamber radius, R_f is the particle bed freeboard radius, and L is the fluidization chamber length. In case the fluidization gas injected via a given gas inlet slot leaves the particle bed when approaching the next gas inlet slot, as experimentally observed by De Wilde [2009]:

$$\langle n \rangle \sim [\text{number of gas inlet slots}]^{-1} \tag{25}$$

The average tangential gas-solid slip factor, <$v^{\tan g}$>/<$u^{\tan g}$>, is determined by the shear resulting from particle-particle and particle-wall collisions and by the tangential gas-solid drag force. In the immediate vicinity of the gas inlet slots, strong variations in its value occur.

Substituting (24) in (20),

$$u^{term} = \left(\frac{2 \cdot F_g \cdot \langle n \rangle \cdot \left(\langle v^{\tan g} \rangle \big/ \langle u^{\tan g} \rangle \right) \sqrt{r}}{\langle \varepsilon_g \rangle \cdot \left(R^2 - R_f^2 \right) \cdot L} \right) \cdot \sqrt{\frac{4 d_p \cdot (\rho_s - \rho_g)}{3 \rho_g \cdot C_D}} \tag{26}$$

At sufficiently high Re_p, (23) can be applied, and the terminal velocity of the particles is seen to be proportional to the fluidization gas flow rate and to the square root of the radial distance from the fluidization chamber central axis. The proportionality factor depends on the gas and solid phase properties and on the fluidization chamber design.

A similar analysis can be derived for the minimum fluidization velocity. Extending the expression of Wen and Yu [1966] to high-G operation:

$$u_{mf} = \frac{Re_{mf} \, \mu}{d_p \rho_g} \tag{27}$$

with:

$$Re_{mf} = \sqrt{C_1^2 + C_2 Ar} - C_1 \tag{28}$$

and:

$$Ar = \frac{d_p^3 \rho_g \left(\rho_s - \rho_g \right) c}{\mu^2} \tag{29}$$

Wen and Yu [1966] found $C_1 = 33.7$ and $C_2 = 0.0408$. Again using relation (24) between the high-G acceleration and the fluidization gas flow rate results in:

$$Ar = \frac{d_p^3 \rho_g \left(\rho_s - \rho_g \right)}{\mu^2} \left(\frac{2 \cdot F_g \cdot \langle n \rangle \cdot \left(\langle v^{\tan g} \rangle \big/ \langle u^{\tan g} \rangle \right)}{\langle \varepsilon_g \rangle \cdot \left(R^2 - R_f^2 \right) \cdot L} \right)^2 r \tag{30}$$

Equation (30) shows that, like the terminal velocity, the minimum fluidization velocity of the particles increases with the fluidization gas flow rate and with the radial distance from the central axis of the fluidization chamber. Figure 4 illustrates the theoretical variation with the fluidization gas flow rate of the minimum fluidization and terminal velocities of the particles in rotating fluidized beds in a static geometry [de Broqueville and De Wilde, 2009]. In the case studied, the radial gas(-solid slip) velocity in the particle bed remained well between the minimum fluidization velocity and the terminal velocity of the particles over the entire fluidization gas flow rate range. Figure 5 shows the corresponding gas-solid heat transfer coefficients that can be obtained. Compared to conventional fluidized beds, rotating fluidized beds in a static geometry easily allow a one order of magnitude intensification of gas-solid heat and mass transfer.
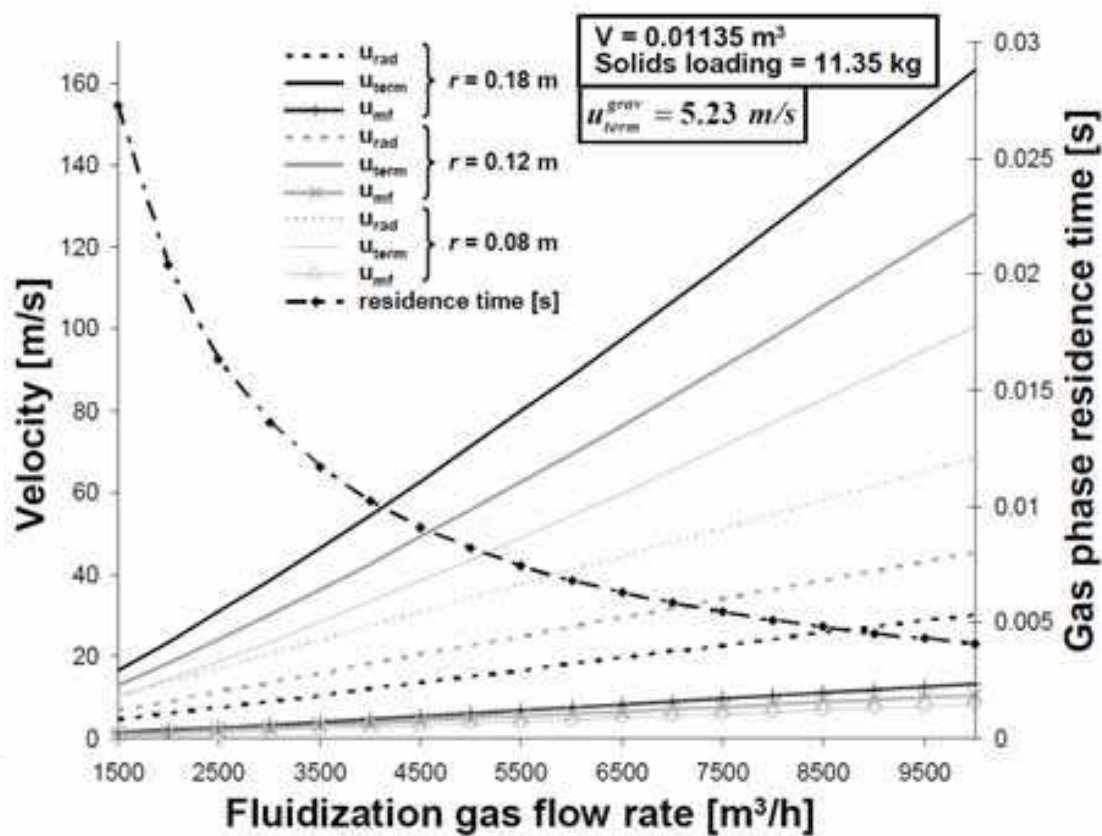

Fig. 4. Theoretical variation with the fluidization gas flow rate of the minimum fluidization and terminal velocities of the particles in rotating fluidized beds in a static geometry. Radial gas(-solid slip) velocity also shown. Conditions: ρ_g = 1.0 kg/m³, ρ_s = 2500 kg/m³, d_p = 700 μm, R = 0.18 m, R_c = 0.065 m, L = 0.135 m, $<\varepsilon_s>$ = 0.4, $<n>$ = 0.042 = 1/24, $<v^{tang}>/<u^{tang}>$ = 0.7. From de Broqueville and De Wilde [2009].

The minimum fluidization and terminal velocities being nearly proportional to the fluidization gas flow rate in rotating fluidized beds in a static geometry results from the counteracting forces - radial gas-solid drag force and solid phase inertial forces - being affected by the fluidization gas flow rate in a similar way. It should be stressed that, as illustrated in Figure 4, this implies a unique flexibility in the fluidization gas flow rate and in the gas-solid slip velocities and related gas-solid heat and mass transfer coefficients at which rotating fluidized beds in a static geometry can be operated.
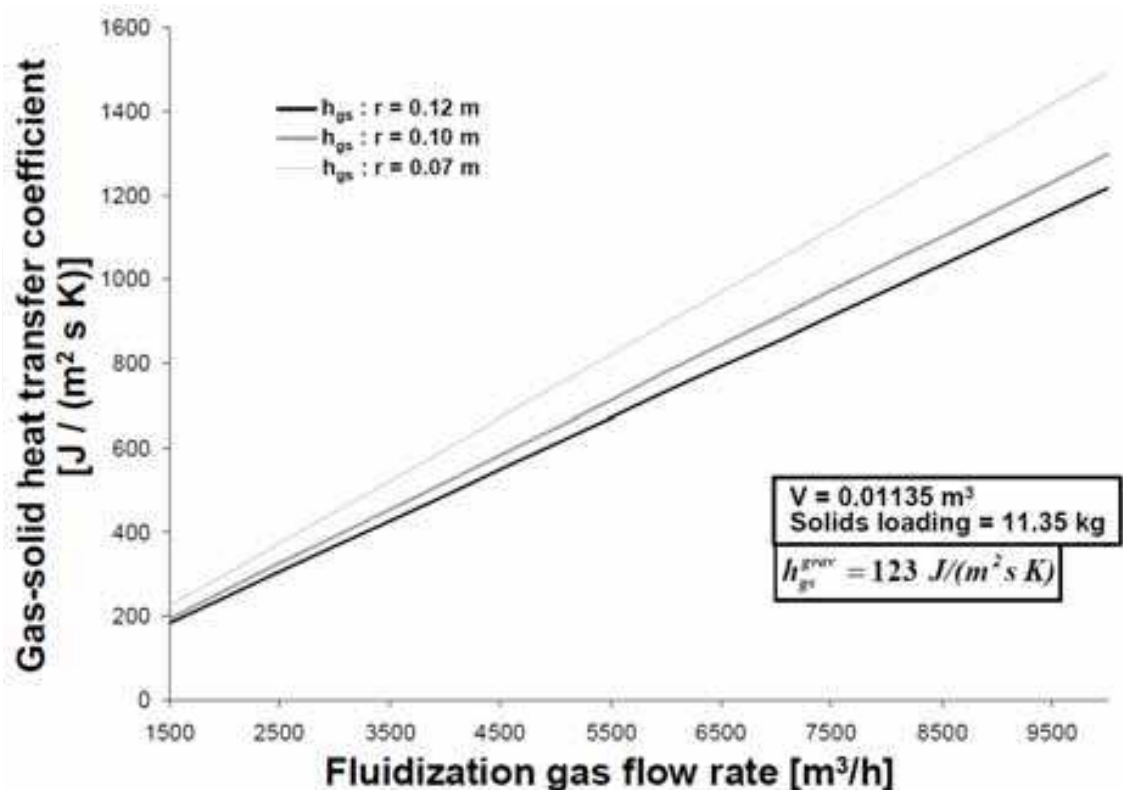
Fig. 5. Theoretical variation with the fluidization gas flow rate of the gas-solid heat transfer coefficient in rotating fluidized beds in a static geometry. Conditions: see Figure 4. From de Broqueville and De Wilde [2009].

4. A computational fluid dynamics evaluation of the intensification of gas-solid heat transfer in rotating fluidized beds in a static geometry

Recent advances in computational power allow detailed three-dimensional simulations of the dynamic flow pattern in fluidized bed reactors. The most popular model is based on an Eulerian approach for both phases, i.e. the gas and the solid phase [Froment et al., 2010]. The solid phase continuity equations, shown in Table 1, are similar to those of the gas phase and can be derived from the Kinetic Theory of Granular Flow (KTGF) [Gidaspow, 1994]. The solid phase physico-chemical properties, like the solid phase viscosity, depend on the so-called granular temperature, a measure for the fluctuations in the solid phase velocity field at the single particle level. Such fluctuations essentially result in collisions between particles. Expressions for the solid phase physico-chemical properties are also obtained from the KTGF - see Gidaspow [1994] for an overview and more references in this field.

Fluctuations in the flow field also occur at the micro-scale. These are related to turbulence. Their calculation requires Direct Numerical Simulations (DNS) or Large-Eddy Simulations (LES) which are extremely time consuming. Therefore, continuity equations which are averaged over the micro-scales, so-called Reynolds-averaged continuity equations, are derived and solved using a Computational Fluid Dynamics (CFD) routine. Additional terms appear in these equations, expressing the effect of the micro-scale phenomena on the larger-scale behavior. These terms have to be modeled. A popular turbulence model is the k-ε model, also shown in Table 1, which has also been extended in different ways to multi-phase flows.

Gas phase mass balance

$$\frac{\partial}{\partial t}(\varepsilon_g \rho_g) + \frac{\partial}{\partial r} \cdot (\varepsilon_g \rho_g \bar{u}) = 0$$

Solid phase mass balance

$$\frac{\partial}{\partial t}(\varepsilon_s \rho_s) + \frac{\partial}{\partial r} \cdot (\varepsilon_s \rho_s \bar{v}) = 0$$

Gas phase momentum balance

$$\frac{\partial}{\partial t}(\varepsilon_g \rho_g \bar{u}) + \frac{\partial}{\partial r} \cdot (\varepsilon_g \rho_g \overline{uu}) = -\frac{\partial}{\partial r}\left(P + \frac{2}{3}\rho_g k\right) - \frac{\partial}{\partial r} \cdot (\varepsilon_g \overline{\overline{s_g}}) - \beta(\bar{u} - \bar{v}) + \varepsilon_g \rho_g \bar{g}$$

with: $\overline{\overline{s_g}} = -\left[\left(\xi_g - \frac{2}{3}\mu_g\right)\left(\frac{\partial}{\partial r} \cdot \bar{u}\right)\overline{\overline{I}} + (\mu_g + \mu_g')\left(\left(\frac{\partial}{\partial r}\bar{u}\right) + \left(\frac{\partial}{\partial r}\bar{u}\right)^T\right)\right]$

Solid phase momentum balance

$$\frac{\partial}{\partial t}(\varepsilon_s \rho_s \bar{v}) + \frac{\partial}{\partial r} \cdot (\varepsilon_s \rho_s \overline{vv}) = -\frac{\partial}{\partial r}P_s - \frac{\partial}{\partial r} \cdot (\varepsilon_s \overline{\overline{s_s}}) + \beta(\bar{u} - \bar{v}) + \varepsilon_s \rho_s \bar{g}$$

with: $\overline{\overline{s_s}} = -\left[\left(\xi_s - \frac{2}{3}\mu_s\right)\left(\frac{\partial}{\partial r} \cdot \bar{v}\right)\overline{\overline{I}} + (\mu_s)\left(\left(\frac{\partial}{\partial r}\bar{v}\right) + \left(\frac{\partial}{\partial r}\bar{v}\right)^T\right)\right]$

Gas phase energy balance

$$\frac{\partial}{\partial t}(\varepsilon_g \rho_g(e_g + k + q_g)) + \frac{\partial}{\partial r} \cdot (\varepsilon_g \rho_g \bar{u}(e_g + k + q_g)) - \frac{\partial}{\partial r} \cdot \left(\varepsilon_g(\lambda + \lambda')\frac{\partial T_g}{\partial r}\right) =$$

$$-\frac{\partial}{\partial r} \cdot \left(\left(P + \frac{2}{3}\rho_g k\right)\bar{u}\right) - \frac{\partial}{\partial r} \cdot (\varepsilon_g \overline{\overline{s_g}} \cdot \bar{u}) - \frac{\beta}{2}((\bar{u} \cdot \bar{u}) - (\bar{v} \cdot \bar{v})) + \varepsilon_g \rho_g \bar{g} \cdot \bar{u} - \varepsilon_s \rho_s a_s h_{gs}(T_g - T_s)$$

Solid phase energy balance

$$\frac{\partial}{\partial t}(\varepsilon_s \rho_s(e_s + q_s)) + \frac{\partial}{\partial r} \cdot (\varepsilon_s \rho_s \bar{v}(e_s + q_s)) - \frac{\partial}{\partial r} \cdot \left(\varepsilon_s \lambda_s \frac{\partial T_s}{\partial r}\right) =$$

$$-\frac{\partial}{\partial r} \cdot (P_s \bar{v}) - \frac{\partial}{\partial r} \cdot (\varepsilon_s \overline{\overline{s_s}} \cdot \bar{v}) + \frac{\beta}{2}((\bar{u} \cdot \bar{u}) - (\bar{v} \cdot \bar{v})) + \varepsilon_s \rho_s \bar{g} \cdot \bar{v} + \varepsilon_s \rho_s a_s h_{gs}(T_g - T_s)$$

Gas phase k-equation

$$\frac{\partial}{\partial t}(\varepsilon_g \rho_g k) + \frac{\partial}{\partial r} \cdot (\varepsilon_g \rho_g \bar{u}k) = \frac{\partial}{\partial r} \cdot \left(\varepsilon_g \frac{\mu_g + \mu_g'}{\sigma_k}\frac{\partial k}{\partial r}\right) + \left[\varepsilon_g \mu_g'\left(\left(\frac{\partial}{\partial r}\bar{u}\right) + \left(\frac{\partial}{\partial r}\bar{u}\right)^T\right)\right] : \left(\frac{\partial}{\partial r}\bar{u}\right) - \varepsilon_g \rho_g \varepsilon$$

Gas phase ε-equation

$$\frac{\partial}{\partial t}(\varepsilon_g \rho_g \varepsilon) + \frac{\partial}{\partial r} \cdot (\varepsilon_g \rho_g \bar{u}\varepsilon) = \frac{\partial}{\partial r} \cdot \left(\varepsilon_g \frac{\mu_g + \mu_g'}{\sigma_\varepsilon}\frac{\partial \varepsilon}{\partial r}\right)$$

$$+ C_{1\varepsilon}\frac{\varepsilon}{k}\left[\varepsilon_g \mu_g'\left(\left(\frac{\partial}{\partial r}\bar{u}\right) + \left(\frac{\partial}{\partial r}\bar{u}\right)^T\right) : \left(\frac{\partial}{\partial r}\bar{u}\right)\right] - C_{2\varepsilon}\varepsilon_g \rho_g \frac{\varepsilon^2}{k}$$

Granular temperature transport equation

$$\frac{3}{2}\left[\frac{\partial}{\partial t}(\varepsilon_s \rho_s \Theta) + \frac{\partial}{\partial r} \cdot (\varepsilon_s \rho_s \bar{v}\Theta)\right] = \frac{\partial}{\partial r} \cdot \left(\varepsilon_s \kappa \frac{\partial}{\partial r}\Theta\right) - (P_s \overline{\overline{I}} + \varepsilon_s \overline{\overline{s_s}}) : \left(\frac{\partial}{\partial r}\bar{v}\right) - \gamma + \beta(q_{12} - 3\Theta)$$

Table 1. Eulerian-Eulerian approach. Continuity equations for each phase.

Such extensions are, however, purely empirical. In gas-solid flows, additional meso-scale structures related to a non-uniform distribution of the particles develop [Agrawal et al., 2001]. Depending on the operating conditions, clusters of particles and gas bubbles are typically observed. Meso-scale structures cover the range from the micro- to the macro-scale, so that there is no separation of scales. The calculation of the dynamics of meso-scale structures is time consuming. Averaging the continuity equations over the meso-scales is theoretically possible, see Agrawal et al. [2001], Zhang and VanderHeyden [2002] and De Wilde [2005, 2007], but modeling the additional terms that appear is challenging. No reliable closure relations exist at this time. Therefore, dynamic simulations using a sufficiently fine spatial and temporal mesh are to be carried out.

Boundary conditions have to be imposed at solid walls. For gas-solid flows, they are usually based on a no-slip behavior for the gas phase and a partial slip behavior for the solid phase. Johnson and Jackson [1987] proposed a model introducing a specularity coefficient and a particle-wall restitution coefficient for which values of 0.2 and 0.9 were used by Trujillo and De Wilde [2010].

	Conventional fluidized bed	Rotating fluidized bed in a static geometry
Gas distribution chamber:	/	Outer diameter [m]: $54 \cdot 10^{-2}$ Number of gas inlets: 12 Gas inlet width [m]: $3.5 \cdot 10^{-2}$
Fluidization chamber:	Width [m]: $15 \cdot 10^{-2}$ Height [m]: $50 \cdot 10^{-2}$ Number of gas inlets: 7 Gas inlet width [m]: $2 \cdot 10^{-3}$	Outer diameter [m]: $36 \cdot 10^{-2}$ Number of tangential gas inlet slots: 24 Gas inlet slot width [m]: $2.3 \cdot 10^{-3}$ Number of solids inlets: 24 Solids inlet slot width [m]: $5 \cdot 10^{-3}$
Chimney:	/	Diameter [m]: $12-13 \cdot 10^{-2}$ Number of outlet slots: 1 Outlet slot width [m]: $8 \cdot 10^{-2}$
Solid particles:	Diameter [m]: $700 \cdot 10^{-6}$ Density [kg/m³]: 2500 Restitution coefficient for particle-particle collisions (e): 0.9 Specularity coefficient for particle-wall collisions (ϕ): 0.2 Initial temperature [K]: 300	
	Mass in the fluidization chamber [kg/m$_{length\ fluid.\ chamber}$]: 33.75	Mass fed* to the fluidization chamber [kg/m$_{length\ fluid.\ chamber}$]: 33.75 *fed during first 5.63 s of the simulation
Fluidization gas:	Flow rate [m³/(h·m$_{length\ fluid.\ chamber}$)]: (a) 195 (b) 540 (c) 1080	Flow rate [m³/(h·m$_{length\ fluid.\ chamber}$)]: (a) 29800 (b) 59600
	Temperature [K]: $300 \rightarrow 400$ at time t_0	

Table 2. Simulation conditions for the CFD step response study of gas-solid heat transfer in gravitational fluidized beds and rotating fluidized beds in a static geometry by de Broqueville and De Wilde [2009].

By means of CFD, de Broqueville and De Wilde [2009] studied the response of the particle bed temperature to a step change in the fluidization gas temperature. Over a range of fluidization gas flow rates, a comparison between gravitational fluidized beds and rotating fluidized beds in a static geometry was made. The simulation conditions are summarized in Table 2. It should be remarked that the fluidization gas flow rate was close to the maximum possible value, i.e. for avoiding particle entrainment by the gas, for the gravitational fluidized bed, but not for the rotating fluidized bed in a static geometry, due to its unique flexibility explained above.
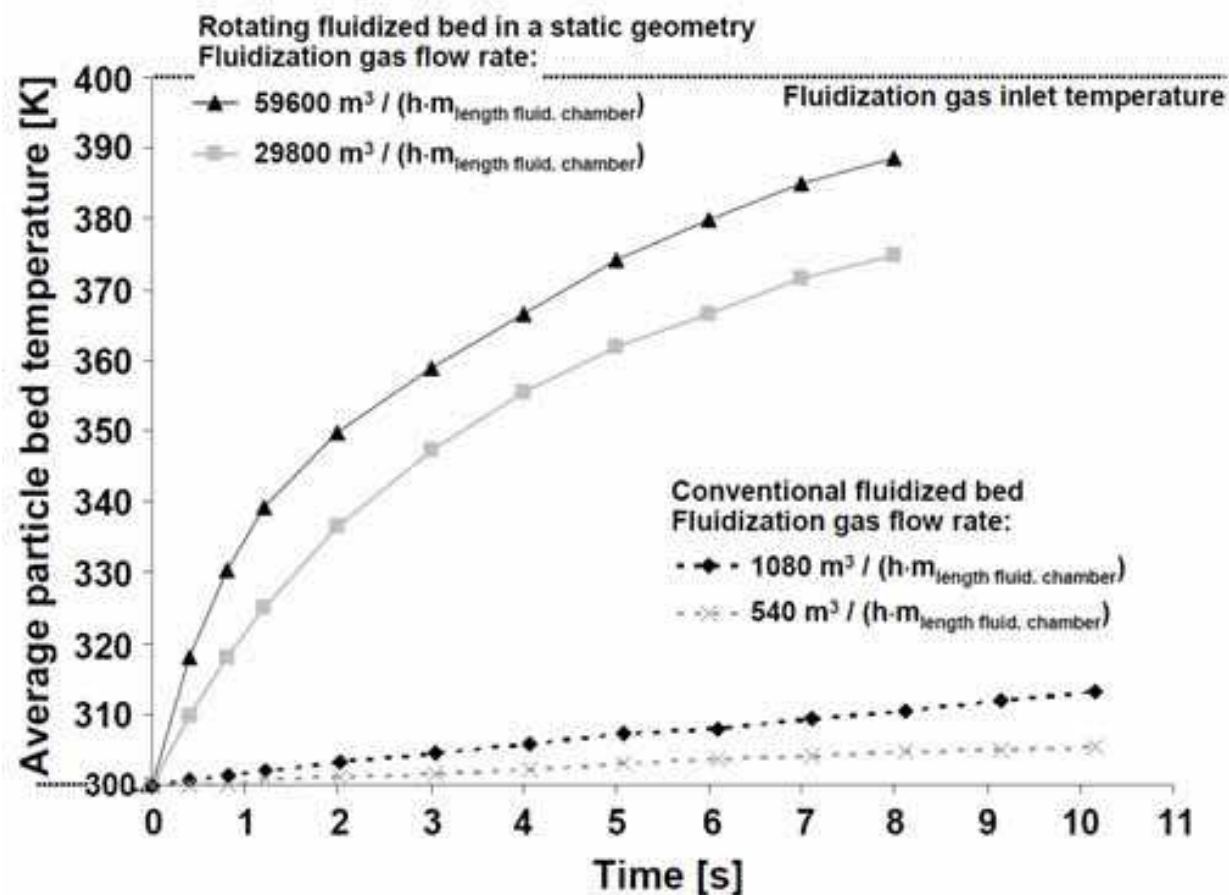
Fig. 6. Response of the average particle bed temperature to a step change in the fluidization gas temperature. Comparison of gravitational fluidized beds and rotating fluidized beds in a static geometry with equal solids loading at different fluidization gas flow rates. Conditions: see Table 2. From de Broqueville and De Wilde [2009].

Figure 6 shows that the particle bed temperature can respond much faster to changes in the fluidization gas temperature in rotating fluidized beds in a static geometry than in gravitational fluidized beds. This is due to a combination of effects. High-G operation allows higher gas-solid slip velocities and, as such, higher gas-solid heat transfer coefficients. The unique flexibility in the fluidization gas flow rate and radial gas-solid slip velocity was demonstrated in Figures 4 and 5. Also, the particle bed is cylindrically shaped in rotating fluidized beds in a static geometry, resulting in a higher particle bed width-to-height ratio than in gravitational fluidized beds. This, combined with the higher allowable radial gas-solid slip velocities, allows much higher fluidization gas flow rates per unit volume particle

bed in rotating fluidized beds in a static geometry than in gravitational fluidized beds. The gas-solid contact is also intensified in rotating fluidized beds in a static geometry as a result of the higher particle bed density and the improved particle bed uniformity, i.e. the absence of bubbles. This is demonstrated in Figure 7, showing the calculated solids volume fraction profiles in both the gravitational fluidized bed and the rotating fluidized bed in a static geometry at the highest fluidization gas flow rates studied.
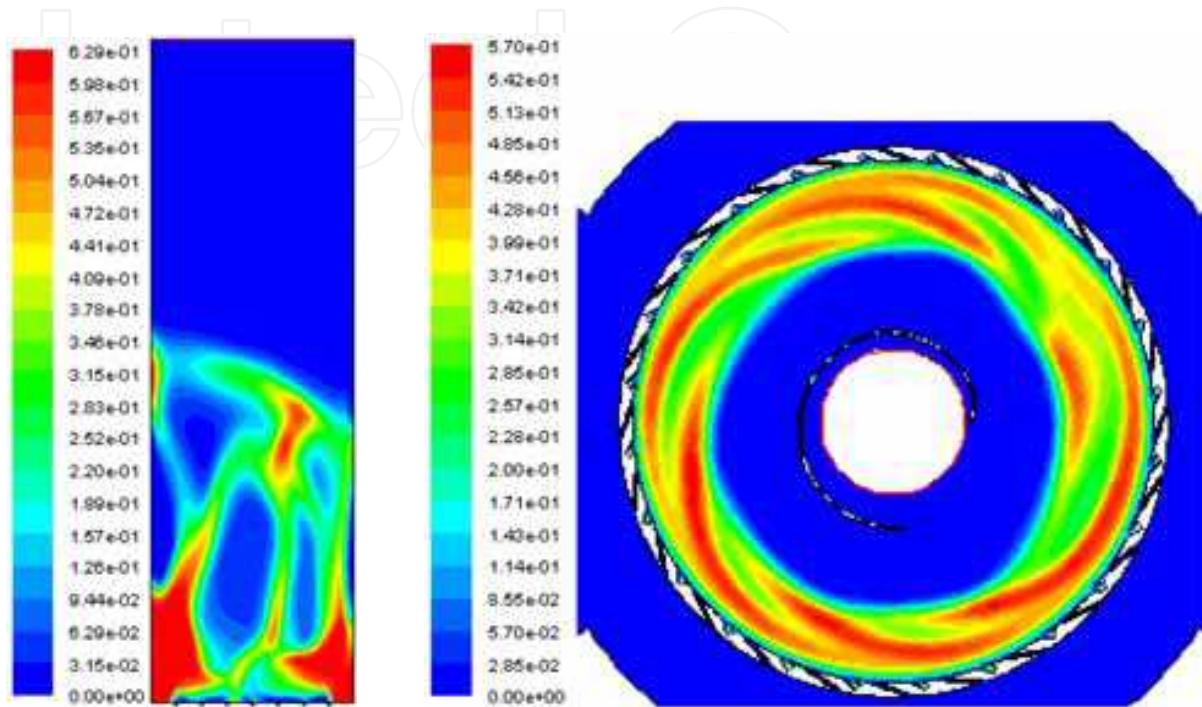
Fig. 7. Calculated solids volume fraction profiles in a gravitational fluidized bed at a fluidization gas flow rate of 1080 m³/(h m_length fluid. chamber) (top) and in a rotating fluidized bed in a static geometry at a fluidization gas flow rate of 59600 m³/(h m_length fluid. chamber) (bottom). Scales shown are different. Conditions: see Table 2. From de Broqueville and De Wilde [2009].

An important feature of rotating fluidized beds in a static geometry is the excellent particle bed mixing. This is reflected in an improved particle bed temperature uniformity, as shown in Figure 8. Such a uniformity may be of particular importance in chemical reactors, where the heat of reaction has to be provided to or removed from the particle bed. This is illustrated in the next section for the Fluid Catalytic Cracking (FCC) process.

5. A computational fluid dynamics study of fluid catalytic cracking of gas oil in a rotating fluidized bed in a static geometry

Fluid Catalytic Cracking (FCC) is a process used in refining to convert heavy Gas Oil (GO) or Vacuum Gas Oil (VGO) into lighter Gasoline (G) and Light Gases (LG). Coke (C) is an inevitable by-product in FCC and is deposited on the catalyst, deactivating it. To restore the catalyst activity, the coke has to be burned off. In view of the reaction and catalyst deactivation time scales, continuous operation requires the catalyst particles to be in a fluidized state, so that they can be easily transported between the cracking reactor and the catalyst regenerator. From the mid-40's on, fluidized bed reactor technology has been
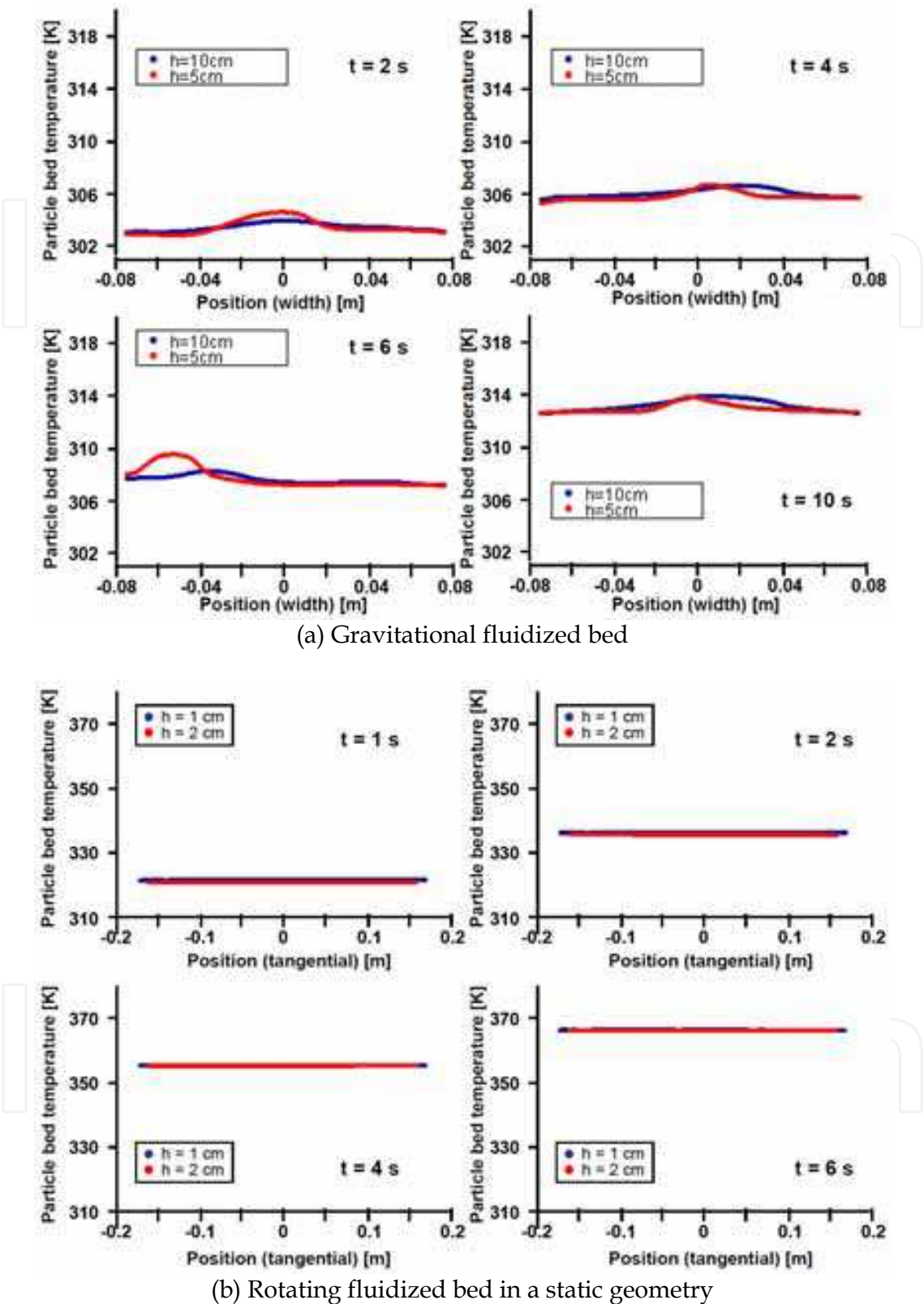
(a) Gravitational fluidized bed

(b) Rotating fluidized bed in a static geometry

Fig. 8. Calculated temperature profiles (a) in a gravitational fluidized bed at a fluidization gas flow rate of 1080 m³/(h m$_{length\ fluid.\ chamber}$) and (b) in a rotating fluidized bed in a static geometry at a fluidization gas flow rate of 29800 m³/(h m$_{length\ fluid.\ chamber}$). Conditions: see Table 2. From de Broqueville and De Wilde [2009].

developed in this context. The process is designed in such a way that the heat of combustion generated by burning off the coke is used for the endothermic cracking reactions, the circulating catalyst being the heat carrier. The original technology made use of a cracking reactor operated in the bubbling or turbulent regime (Figure 1). As catalysts became more active, riser reactors were introduced.

FCC riser reactors are 30 to 40 m tall with a diameter of typically 0.85 m. Operating in the riser regime, the particle bed density is low, with typically a solids volume fraction below 5%. The catalyst leaving the riser reactor is separated from the gaseous product in cyclones and goes via a stripper section to the regenerator. Partial or complete combustion of the coke is possible, depending on the feed cracked and the resulting coke formation and the energy requirements for the cracking reactions. The regenerated catalyst is returned to the riser via standpipes by the action of gravity. A sufficient standpipe height is required and this on its turn imposes a certain riser height. The cracking temperature in the riser reactor is limited to avoid over-cracking and temperature non-uniformities.

Significant intensification of the FCC process is possible. The particle bed density can be drastically increased, that is, by a factor 10. To avoid over-cracking under such conditions, the gas phase residence time has to be sharply decreased. This can be done by increasing the gas phase velocity, reducing the particle bed height, or a combination of these. Also the gas-solid heat transfer has to be intensified. This is possible by increasing the gas-solid slip velocity. Finally, to avoid temperature non-uniformities, the particle bed mixing can be improved. From the previous Sections 3 and 4, the potential of rotating fluidized beds for intensifying the FCC process is clear. Important challenges do, however, remain. Some of these were addressed by Trujillo and De Wilde [2010], who in particular demonstrated that sufficiently high conversions can be achieved in rotating fluidized beds in a static geometry. Furthermore, a one order of magnitude process intensification was predicted.
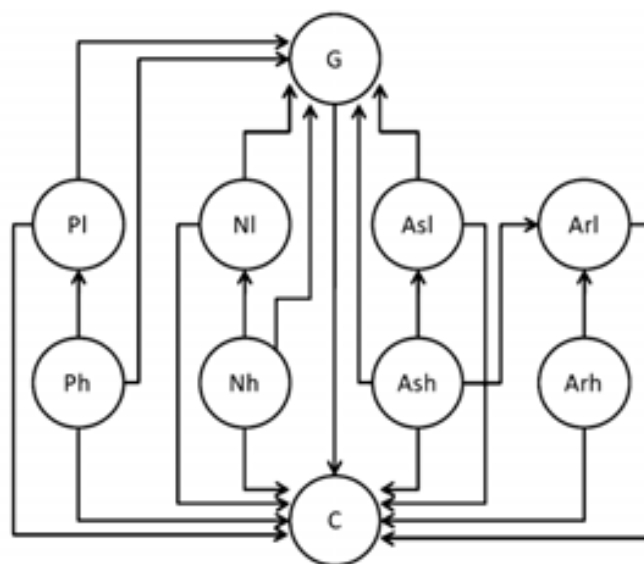

Fig. 9. Ten-lump model for the catalytic cracking of gas oil [Jacob et al., 1976].

The CFD simulations by Trujillo and De Wilde [2010] made use of the Eulerian-Eulerian approach already described in Section 4. The basic set of continuity equations, shown in Table 1, has to be extended to account for the reactions between different species. The catalytic cracking of gas oil was described by a 10-lump model, shown in Figure 9 [Jacob et

al., 1976]. The C-lump is a mixture of coke and light gases (C_1 - C_4). The effects of the adsorption of heavy aromatics and of catalyst deactivation by coke on the reaction rates were accounted for. Two-dimensional periodic domain simulations of a 12-slot, 1.2 m diameter, polygonal body RFB-SG type reactor were carried out and a comparison with a 30 m tall riser was made. Details on the simulation model and on the reactor geometries simulated can be found in Trujillo and De Wilde [2010].
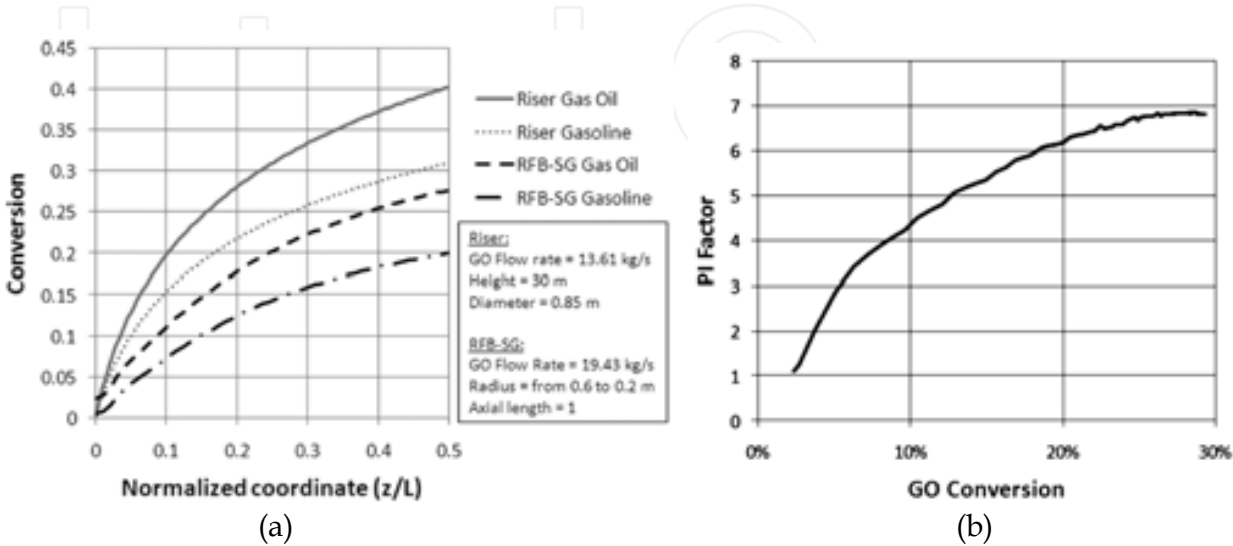

Fig. 10. FCC process intensification using rotating fluidized beds in a static geometry. Comparison with riser technology. (a) Gas Oil conversion as a function of the normalized coordinate; (b) Intrinsic process intensification factor as a function of the Gas Oil conversion. Conventional cracking catalyst and cracking temperature of 775 K. From Trujillo and De Wilde [2010].
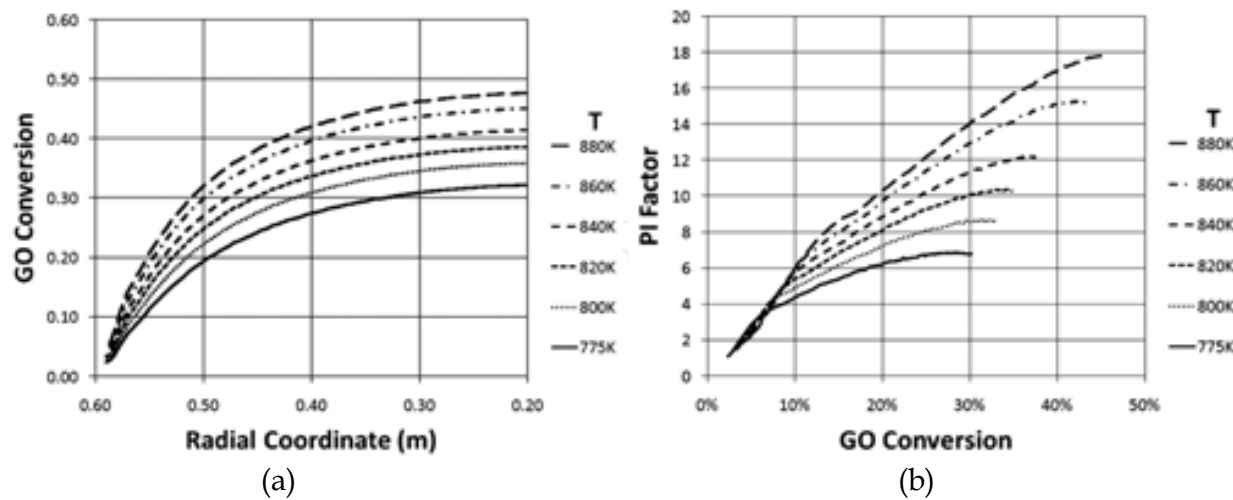

Fig. 11. FCC process intensification using rotating fluidized beds in a static geometry at increased cracking temperatures. Comparison with conventional riser technology. (a) Gas Oil conversion in the RFB-SG as a function of the radial coordinate; (b) Process intensification factor as a function of the Gas Oil conversion for different cracking temperatures. Conventional cracking catalyst and cracking temperature of 775 K. From Trujillo and De Wilde [2010].

The simulations first focused on the intrinsic process intensification potential of rotating fluidized beds in a static geometry, that is, operating at cracking temperatures and with the same catalyst used in riser reactors. Figure 10 shows the gas oil conversion as a function of the normalized coordinate and the intrinsic process intensification factor as a function of the gas oil conversion for a non-optimized RFB-SG reactor design.

With an optimized geometry, intrinsic process intensification by one order of magnitude can be easily achieved. Furthermore, due to the improved temperature uniformity in the particle bed, operation at higher cracking temperatures or working with a ore active catalyst is possible. Simulations at higher cracking temperatures, for example, shown in Figure 11, showed that process intensification by a factor 20 is within reach. This nicely illustrates the advantage that can be taken from the increased gas-solid mass and heat transfer coefficients and the improved particle bed density and uniformity in rotating fluidized beds in a static geometry.

6. Experimental evaluation of the intensification of drying of granular material in rotating fluidized beds in a static geometry

The intensification of gas-solid mass and heat transfer in rotating fluidized beds in a static geometry should allow intensifying the drying of granular material. Eliaers and De Wilde [2010] compared drying of biomass particles in a conventional fluidized bed and in a rotating fluidized bed in a static geometry. Batch and continuous flow experiments were carried out. The fluidization chamber dimensions and the operating conditions for the continuous flow experiments are summarized in Table 3.

	Conventional fluidized bed	Rotating fluidized bed in a static geometry
Dimensions	D = 0.10 m H = 2.00 m	D = 0.43 m D(chimney) = 0.10 m L = 0.24 m
Gas distribution	Cone and perforated plate	72, 30° inclined gas inlet slots
Solids feeding	Via side wall at h = m	Via end plate
Particle characteristics	Pelletized wood, cylindrically shaped, d_p = 4 mm, h_p = 4 mm	
Operating conditions		
T [K]	318	
P_{out} [Pa]	101300	
Gas mass flow rate [Nm³/h]	110	700
Solids mass flow rate [g wet solids / s]	1, 2, 3, 6, 9	3, 6, 9, 12, 15, 18
Solids inlet humidity [g water / kg dry solids]	850	

Table 3. Comparison of the drying of biomass particles in a conventional fluidized bed and in a rotating fluidized bed in a static geometry. Fluidization chamber dimensions and operating conditions.

The pelletized wood particles have mainly macro-pores, so that intra-particle diffusion limitations are not expected to be dominant in the range of drying conditions studied.
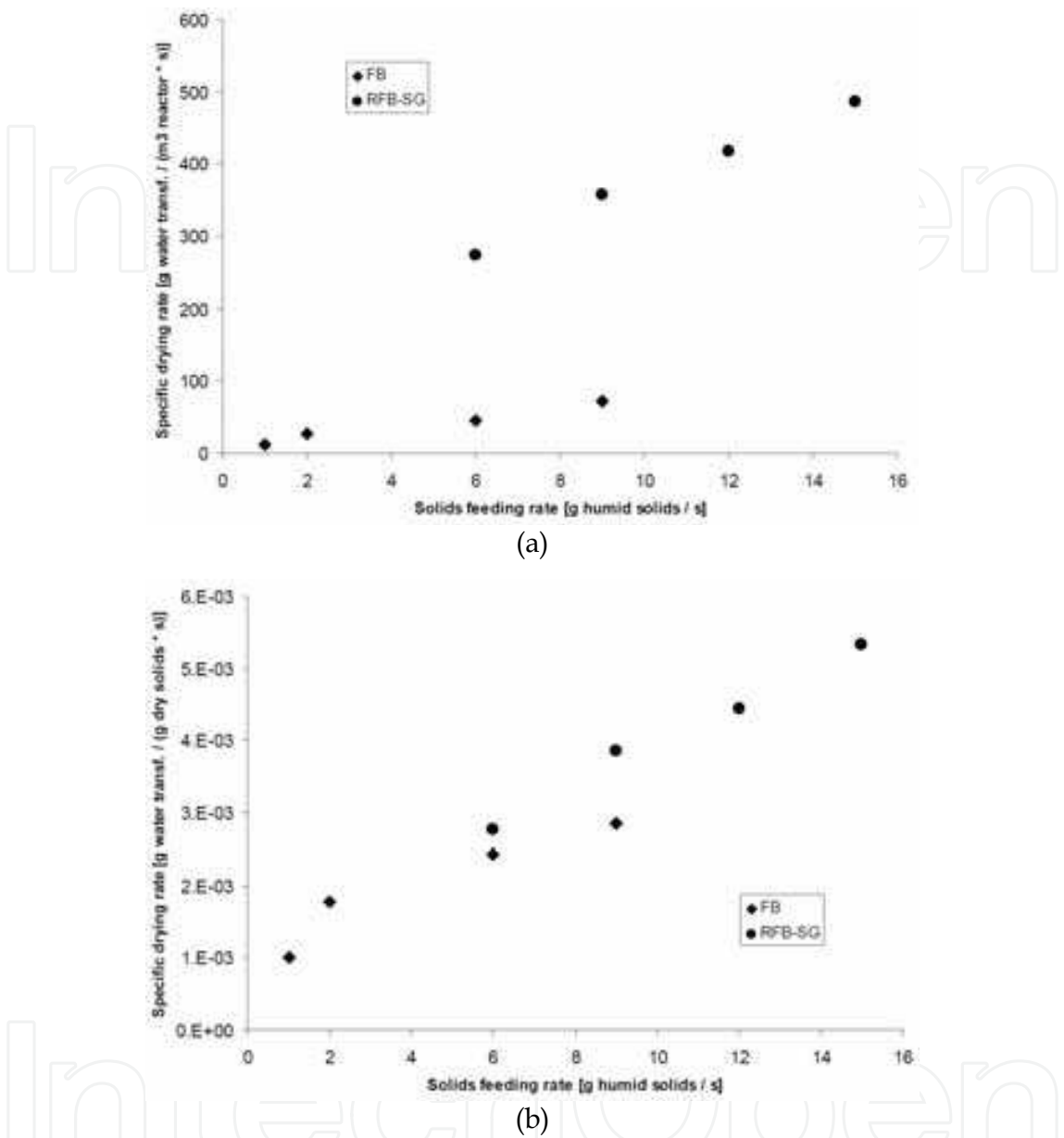

(a)

(b)

Fig. 12. Comparison of drying of biomass particles in a gravitational fluidized bed and in a rotating fluidized bed in a static geometry. (a) Specific drying rate in g water transferred per m3 reactor and per second as a function of the solids feeding rate; (b) Specific drying rate in g water transferred per g dry solids and per second as a function of the solids feeding rate. Fluidization chamber dimensions and operating conditions: see Table 3. From Eliaers and De Wilde [2010].

Intensification of the drying process can be due to an increased particle bed density and improved particle bed uniformity, on the one hand, and increased gas-solid mass and heat transfer coefficients, on the other hand. For the conditions studied, the value of the gas-solid mass and heat transfer coefficients are comparable in the gravitational fluidized bed and in the RFB-SG. The gas-solid slip velocity in both the gravitational and the rotating fluidized

bed in a static geometry is around 4.7 m/s. Hence the intensification comes exclusively from the increased particle bed density and improved particle bed uniformity. Accounting for mean particle bed solids volume fractions of about 4 % in the gravitational fluidized bed and about 25 % in the RFB-SG, there is a theoretical process intensification potential of easily a factor 6. When operating the RFB-SG at higher fluidization gas flow rates, further intensification of the drying process resulting from increased gas-solid mass and heat transfer coefficients may be achieved.
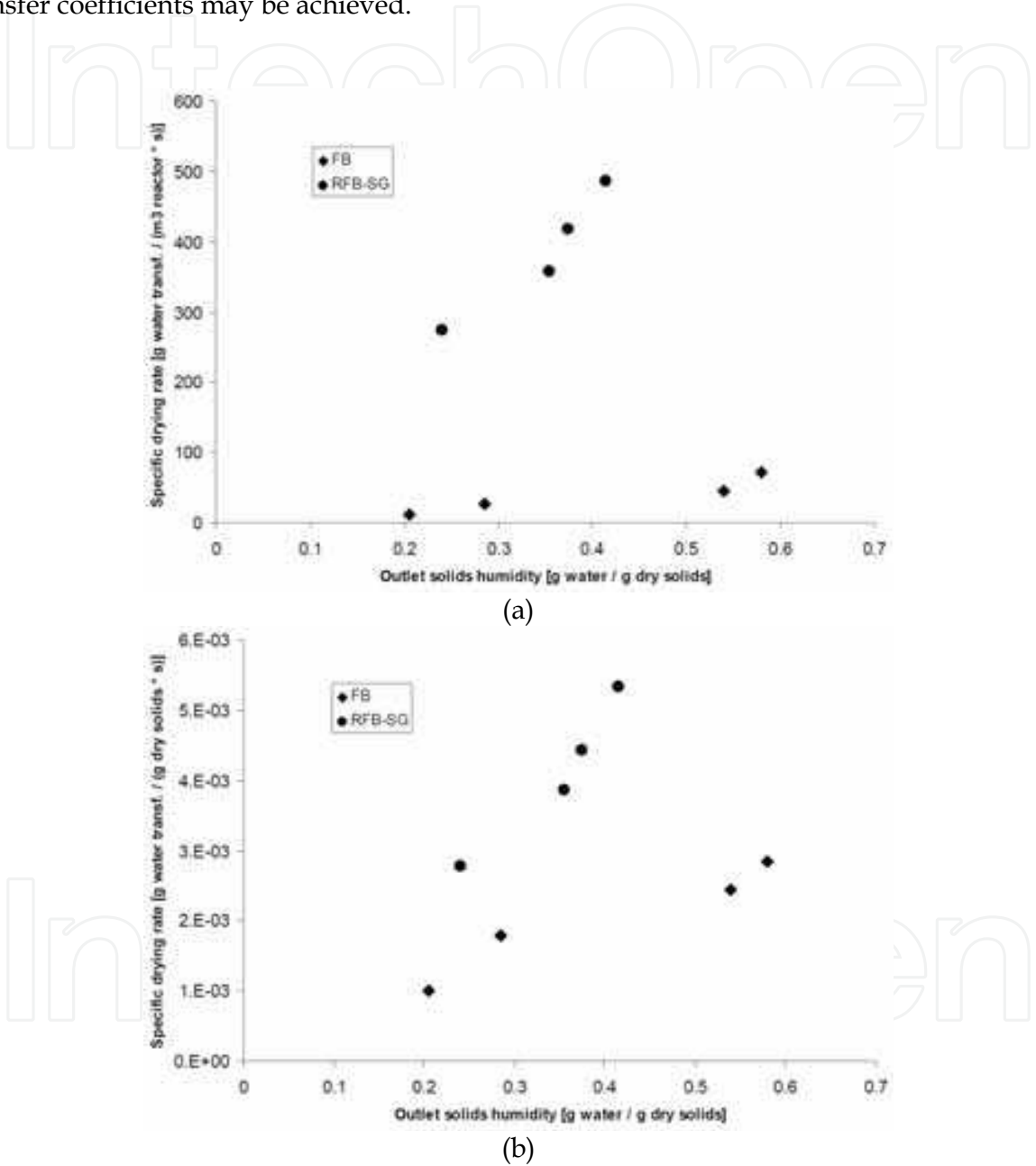

(a)

(b)

Fig. 13. Comparison of drying of biomass particles in a gravitational fluidized bed and in a rotating fluidized bed in a static geometry. Evaluation of the process intensification factor. (a) Specific drying rate in g water transferred per m3 reactor and per second as a function of the outlet solids humidity; (b) Specific drying rate in g water transferred per g dry solids and per second as a function of the outlet solids humidity. Fluidization chamber dimensions and operating conditions: see Table 3. From Eliaers and De Wilde [2010].

Figures 12 and 13 compare the specific drying rates in the gravitational fluidized bed and the RFB-SG, expressed in g water transferred per second and either per m3 reactor (a) or per g dry solids (b), respectively as a function of the solids feeding rate or as function of the outlet solids humidity. The specific drying rate expressed per g dry solids allows evaluating the process intensification due to increased gas-solid slip velocities and the improved particle bed uniformity. The specific drying rate expressed per m3 reactor then allows evaluating the additional process intensification due to the increased particle bed density. Evaluation of the process intensification is best done at equal outlet solids humidity as shown in Figure 13. The biomass drying process intensification in RFB-SGs is logically the most pronounced at higher outlet solids humidity. With decreasing outlet solids humidity, intra-particle diffusion grows in importance. Figure 13(b) shows that in the range of conditions studied, the improved particle bed uniformity in the RFB-SG results in process intensification with between a factor 2 and 4. As seen from Figure 13(a), the increased particle bed density in the RFB-SG results in additional process intensification and a global process intensification factor of between 10 and 16. As mentioned previously, the process intensification resulting from the use of a RFB-SG can be further increased by operating at higher fluidization gas flow rates.

7. Chapter summary

A theoretical analysis of gas-solid mass and heat transfer shows a significant potential for fluidized bed process intensification by replacing earth gravity with a stronger acceleration. In rotating fluidized beds, the inertia of the solid particles is used to achieve high-G operation. A new type of rotating fluidized bed, i.e., in a static geometry, is studied in this chapter. The rotating motion of the particle bed is generated by the tangential injection of the fluidization gas in the fluidization chamber, via multiple gas inlet slots. A unique flexibility in the fluidization gas flow rate results from the counteracting radial gas-solid drag force and solid phase inertial forces being affected by the fluidization gas flow rate in a similar way. A significant process intensification potential is theoretically expected, resulting from, on the one hand, an increased particle bed density and improved particle bed uniformity and, on the other hand, increased gas-solid mass and heat transfer coefficients. Furthermore, the intense particle bed mixing results in significantly improved particle bed temperature uniformity. Computational Fluid Dynamics (CFD) simulations confirm these promising characteristics of rotating fluidized beds in a static geometry. Application to fluid catalytic cracking (FCC) and to biomass drying is discussed. In FCC, the use of a rotating fluidized bed in a static geometry allows intrinsic process intensification by one order of magnitude. Additional process intensification can be achieved by operating at higher cracking temperatures, which becomes possible due to the improved particle bed temperature uniformity. The use of a more active catalyst can also be considered. Experimental data on drying of biomass particles confirm the theoretically expected process intensification potential. Again, process intensification by one order of magnitude can be easily achieved.

8. Acknowledgments

Notations

a_s	external particle surface area per unit mass particle	[m²/kg solid]
C_t	total molar concentration of active sites	[kmol / kg cat.]
c	acceleration of high-gravity field	[m / s²]
c_p	specific heat of fluid at constant pressure	[kJ/kg K]
D_{Am}	molecular diffusivity for A in a multicomponent mixture	[m_f^3 / m_f s]
d_p	particle diameter	[m]
e_g	gas phase internal energy	[kJ kg⁻¹]
e_s	solid phase internal energy	[kJ kg⁻¹]
F_g	fluidization gas flow rate;	[m³ s⁻¹]
	in 2D, per unit length fluidization chamber	[m_g^3/(h $m_{length\ fluid.\ chamber}$)]
G	superficial mass flow velocity;	[kg / m_r^2 s]
g	acceleration of gravity	[m / s²]
h_f , h_{gs}	heat transfer coefficient for film surrounding a particle	[kJ / m_P^2 s K]
j_D	j-factor for mass transfer	
j_H	j-factor for heat transfer	
k	gas phase turbulent kinetic energy	[kJ kg⁻¹]
k_g^0	mass transfer coefficient in case of equimolar counterdiffusion	[m_f^3 / m_is]
L	length of the fluidization chamber	[m]
L	film thickness	[m]
M_m	mean molecular mass	[kg/kmol]
N_A	molar flux of A with respect to fixed coordinates	[kmol/m² s]
<n>	average number of rotations of the fluidization gas in the particle bed	
P	gas phase pressure	[Pa]
P_s	solid phase pressure	[Pa]
Pr	Prandtl number, $c_p \mu / \lambda$	
q_g	gas phase kinetic energy	[kJ kg⁻¹]
q_s	solid phase kinetic energy	[kJ kg⁻¹]
Q, Q_{gs}	gas-solid heat transfer	[kJ/(s $m_{reactor}^3$)]
r	radial distance from the center of the fluidization chamber	[m]
$\underline{r}$	position vector	
R	Outer fluidization chamber radius	[m]
R_f	Particle bed freeboard radius	[m]
R_c	Chimney radius	[m]
$\underline{\underline{Sc}}$	Schmidt number, μ/ρD	
$\underline{\underline{s}}$	viscous stress tensor	[kg m⁻¹ s⁻²]
T	temperature	[K]
T_s^s	temperature inside solid, resp. at solid surface	[K]
t	time	[s]
u	gas phase velocity	[m/s]
V	volume of the fluidization chamber	[m³]
v	solid phase velocity	[m/s]
y_A, y_B	mole fraction of species A, B …	
β	drag coefficient	[kg m⁻³ s⁻¹]
γ	dissipation of kinetic fluctuation energy by inelastic particle-particle collisions	
		[kg m_r^{-1} s⁻³]

ε	dissipation of turbulent kinetic energy of the gas phase	$[m_r^2 \ s^{-3}]$
ε_g	gas phase volume fraction	$[\ m_g^3 \ / \ m_r^3 \ ]$
ε_s	solid phase volume fraction	$[\ m_s^3 \ / \ m_r^3 \ ]$
Θ	granular temperature	$[kJ/kg]$
κ	granular temperature conductivity	$[kg \ m^{-1} \ s^{-1}]$
λ	thermal conductivity	$[kJ/m \ s \ K]$
μ	dynamic viscosity	$[kg/m \ s]$
ω	angular velocity	$[rad \ s^{-1}]$
ρ_f	fluid density	$[\ kg \ / \ m_f^3 \ ]$
ρ_g	gas density	$[\ kg \ / \ m_G^3 \ ]$
ρ_s	density of catalyst	$[\ kg \ cat. \ / \ m_p^3 \ ]$

Subscript / superscript

g	gas phase
p	particle
s	solid phase
r	radial
rad	radial
t, tang	tangential
term	terminal

9. References

Agrawal, K., Loezos, P.N., Syamlal, M., and Sundaresan, S., J. Fluid Mech., 445, 151 (2001).

Anderson, L.A., Hasinger, S., and Turman, B.N., A.I.A.A. paper, 71, 637 (1971).

Balakrishnan, A.R., and Pei, D.C.T., Can. J. Chem. Eng., 53, 231 (1975).

Chen, Y.-M., A.I.Ch.E. J., 33 (5), 722 (1987).

de Broqueville, A., 2004. Belgian Patent 2004/0186, Internat. Classif. : B01J C08F B01F; publication number: 1015976A3.

de Broqueville, A., De Wilde, J., Chem. Eng. Sci., 64 (6), 1232 (2009).

De Wilde, J., Physics of Fluids, 17:(11), Art. No. 113304 (2005).

De Wilde, J., Physics of Fluids, 19:(5), 058103 (2007).

De Wilde, J., de Broqueville, A., A.I.Ch.E. J., 53 (4), 793 (2007).

De Wilde, J., de Broqueville, A., Powder Technol., 183 (3), 426 (2008).

De Wilde, J., de Broqueville, A., A.I.Ch.E. J., 54 (8), 2029 (2008b).

De Wilde, J., proc., OA70, North American Catalysis Society, 21st National (North American) Annual Meeting (21st NAM), San Francisco, CA, USA, June 7-12 (2009).

Eliaers, P., De Wilde, J., UCL report 270810 (2010).

Fan, L.T., Chang, C.C., Yu, Y.S., Takahashi, T., Tanaka, Z., A.I.Ch.E. J., 31 (6), 999 (1985).

Folsom, B.A., PhD thesis, California Institute of Technology (1974).

Froment, G.F., Bischoff, K.B., and De Wilde, J., Chemical Reactor Analysis and Design, Third edition, Wiley (2010).

Gidaspow, D., Multiphase Flow and Fluidization: Continuum and Kinetic Theory Descriptions, Academic Press (1994).

Jacob, S.M., Gross, B., Voltz, S.E., Jr. V.W. W., A.I.Ch.E. J., 22, 701 (1976).

Johnson, P.C., Jackson, R., J. Fluid Mech., Digital Archive, 176, 67 (1987).

Kochetov, L.M., Sazhin, B.S., Karlik, E.A., Khimicheskoe i Neftyanoe Mashinostroenie, 2, 10 (1969).

Perry, R.H., Chilton, C.H., Chemical Engineers Handbook, 6th ed., McGrawHill, NY (1984).

Qian, G.-H., Bagyi, I., Burdick, I.W., Pfeffer, R., Shaw, H., Stevens, J.G., A.I.Ch.E. J., 47 (5), 1022 (2001).

Quevedo, J.A., Nakamura, H., Shen, Y., Dave, R.N., Pfeffer, R., Proceedings of AIChE Annual meeting 2005, Cincinnati, OH, USA (2005).

Schlünder, E.U., in Chemical Reaction Engineering Reviews-Houston, ed. by D. Luss and V.W. Weekman, A.C.S. Symp. Series, 72, Washington, D.C. (1978).

Squires, A. M., Kwauk, M., and Avidan, A. A., Science, 230 (4732), 1329 (1985).

Watano, S., Imada, Y., Hamada, K., Wakamatsu, Y., Tanabe, Y., Dave, R.N., Pfeffer, R., Powder Technol. 131 (2-3), 250 (2003).

Wen, Y.C., Yu, Y.H., Chem. Eng. Progr. Symp. Ser., 62 (62), 100 (1966).

Zhang, D.Z., VanderHeyden, W.B., Int. J. Multiphase Flow, 28 (5), 805 (2002).
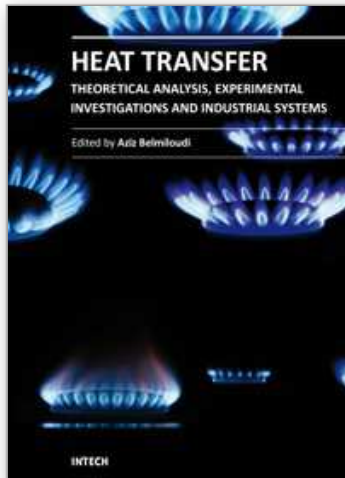
**Heat Transfer - Theoretical Analysis, Experimental Investigations
and Industrial Systems**

Edited by Prof. Aziz Belmiloudi

Over the past few decades there has been a prolific increase in research and development in area of heat transfer, heat exchangers and their associated technologies. This book is a collection of current research in the above mentioned areas and discusses experimental, theoretical and calculation approaches and industrial utilizations with modern ideas and methods to study heat transfer for single and multiphase systems. The topics considered include various basic concepts of heat transfer, the fundamental modes of heat transfer (namely conduction, convection and radiation), thermophysical properties, condensation, boiling, freezing, innovative experiments, measurement analysis, theoretical models and simulations, with many real-world problems and important modern applications. The book is divided in four sections : "Heat Transfer in Micro Systems", "Boiling, Freezing and Condensation Heat Transfer", "Heat Transfer and its Assessment", "Heat Transfer Calculations", and each section discusses a wide variety of techniques, methods and applications in accordance with the subjects. The combination of theoretical and experimental investigations with many important practical applications of current interest will make this book of interest to researchers, scientists, engineers and graduate students, who make use of experimental and theoretical investigations, assessment and enhancement techniques in this multidisciplinary field as well as to researchers in mathematical modelling, computer simulations and information sciences, who make use of experimental and theoretical investigations as a means of critical assessment of models and results derived from advanced numerical simulations and improvement of the developed models and numerical methods.

How to reference

In order to correctly reference this scholarly work, feel free to copy and paste the following:

Juray De Wilde (2011). Gas-Solid Heat and Mass Transfer Intensification in Rotating Fluidized Beds in a Static Geometry, Heat Transfer - Theoretical Analysis, Experimental Investigations and Industrial Systems, Prof. Aziz Belmiloudi (Ed.), ISBN: 978-953-307-226-5, InTech, Available from: http://www.intechopen.com/books/heat-transfer-theoretical-analysis-experimental-investigations-and-industrial-systems/gas-solid-heat-and-mass-transfer-intensification-in-rotating-fluidized-beds-in-a-static-geometry

INTECH
open science | open minds

51000 Rijeka, Croatia

Phone: +385 (51) 770 447

Fax: +385 (51) 686 166

www.intechopen.com

中国上海市延安西路65号上海国际贵都大饭店办公楼405单元

Phone: +86-21-62489820

Fax: +86-21-62489821